Complex, Dynamic Behavior of Extremely Asymmetric Di-*n*-Alkylphosphate-Anion Aggregates, the Long-Chain Effect and the Role of a Limiting Size: Cryo-TEM, SANS, and X-Ray Diffraction Studies

Daphne Weihs,[†] Ellina Kesselman,[‡] Judith Schmidt,[‡] Yeshayahu Talmon,[*,‡] Sonoko Sasuga,[§] Takeshi Fujita,[§] Ken-Ichi Izawa,[⊥] Charmian J. O'Connor,[∥] and Hiro-Fumi Okabayashi[*,§]

[†]Department of Biomedical Engineering, Technion-Israel Institute of Technology, Haifa 3200003, Israel

[‡]Department of Chemical Engineering, Technion-Israel Institute of Technology, Haifa 3200003, Israel

[§]Department of Applied Chemistry, Nagoya Institute of Technology, Gokiso, Showa-ku, Nagoya 466-8555, Japan

[⊥]International Division, Fuji-Silysia Chemical LTD., Nagoya International Center, BLDG 23F 1-47-1, Nagano, Nakamura-ku, Nagoya, Aichi 450-0001, Japan

[∥]Department of Chemistry, The University of Auckland, Private Bag 92019, Auckland 1142, New Zealand

ABSTRACT: For extremely asymmetric *n*-hexyl(*n*-decyl)-phosphate (HDeP), *n*-hexyl(*n*-dodecyl)phosphate (HDoP), and *n*-hexyl(*n*-cetyl)phosphate (HCeP), the effect of the long-chains on the dynamic behavior of their aggregate structures in water was examined by cryo-TEM imaging, SANS, and X-ray diffraction techniques. The cryo-TEM images demonstrated the complex and dynamic behavior of the aggregates, and its dependence on the length of the long-chain. Application of the one-dimensional aggregate theory to the SANS results led to the conclusion that the existence of a limiting size also depended on the length of the main long-hydrocarbon chain and affected strongly the dynamic behavior of the aggregates, causing breakage of thread-like micelles or ribbon-like aggregates. The X-ray diffraction patterns of the lyotropic liquid crystalline samples of HDeP and HCeP were used to estimate the aggregate structures of this limited size.
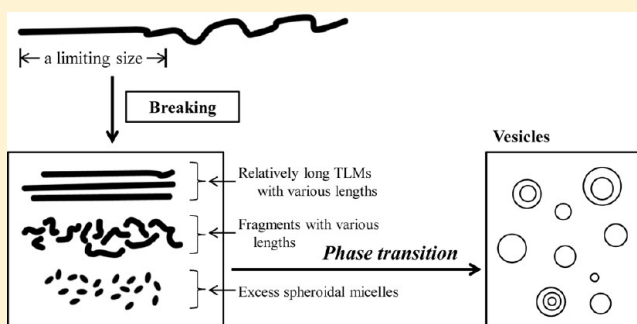
INTRODUCTION

Considerable attention has been given to structural studies of a variety of aggregates formed by surfactant molecules, such as liquid crystals, micelles, vesicles, and lamellae.[1−4] Many studies have played a critical role in elucidating the physical properties of such aggregates. In particular, slow relaxation processes in self-organized systems, such as the so-called "complex liquids", have continued to attract interest, although simple theoretical approaches, like the scaling arguments of de-Gennes,[5] have led to greater understanding of those complex systems. Computer simulations[6] have become very popular in the field of complex liquids, and are now a powerful tool for elucidating these complex systems.

Extensive studies of dynamic surface phenomena within a time scale ranging from 10^{-3} to 10^3 s have been carried out in self-organized systems formed at the air−water or oil−water interface.[7] Changes in surface-tension in self-organized systems of surfactants with low molecular weight usually occur in less than 1 s.[7] However, a slow surface-tension equilibration in micellar solutions of di-*n*-alkyl-sulfosuccinates could not be interpreted solely on the basis of diffusion on the surface.[8] Furthermore, a similarly slow surface-tension variation and a

simultaneous increase in the surface dilatational modulus, observed for very pure samples of sodium di-*n*-heptyl-sulfosuccinate (SDHpS), have been ascribed to a cooperative ordering phenomenon on the surface.[9] The effect of such surface properties on the formation of a three-dimensional structure, similar to that of a lamellar liquid crystal, has been studied by Franses et al.[10] They suggested that the observed variation in surface-tension is a reflection of the change in aggregate nanostructure on the surface.

As is well-known, self-organized systems appear spontaneously as dissipative structures in the nonlinear domain, far from equilibrium.[11] Recently, Sumino et al.[12] have examined the irregular deformation of a mm-size oil droplet, formed in an oil−water system with binary surfactants, which was attributed to dissipative processes caused by formation and breakage of aggregates on the oil−water interface. They also used small-angle X-ray scattering to investigate the structures of aggregates

formed at the oil–water interface, thereby indicating that highly ordered lamellar structures were formed at the interfaces.

In a freshly prepared normal or reversed surfactant micellar system, ordering of the bilayer-structure formed at the oil/water interface should occur cooperatively until the membrane-structure reaches its final ordered state. This concept implies that there is a difference in the aggregation structure of freshly prepared and aged interfaces. Previous studies of phase behavior of reversed micelle systems[13−17] have focused on the final ordered structures, a limitation imposed by the fast rate of attaining the final ordered state. Interpretation of such an ordering process at the molecular level is very rare, in spite of the importance of its practical applications.

The difference in aggregation structure between the freshly prepared and aged samples, in the sodium dioleyl-sulfosuccinate (SDOleS)–decane–water system, has been examined by the SAXS.[18] The time-dependent SAXS profiles provided evidence that the droplet-lamellar transition occurs spontaneously, but very slowly at 298 K, and depends on the quantity of water solubilized into the microemulsion. The dynamic models of AOT-reversed micelles[19] and the crystal structures of the AOT-homologues[9] were used successfully to explain the aggregation behavior.

The very slow surface-tension equilibration in the SDHpS aqueous solution[9] and the spontaneous droplet-lamellar transition in the SDOleS–decane–water system[18] may be ascribed to the molecular-skeleton characteristic of these surfactants as the common structural unit of the asymmetric succinate-skeleton (O$_3$S-CH(CH$_2$-COO-R$_1$)-COO-R$_1$, R$_1$: n-alkyl group), possibly leading to the difference in the aggregation behavior between freshly prepared and aged interfaces. The effect of the spontaneous curvature of the oil–water interface[18−20] formed by the succinate-surfactant systems may play an important role.

Symmetric di-n-alkylphosphates (DAPs) have proved to be suitable as model systems for further study of the dynamic change in interactions between phospholipids and solvent (water).[20] Further understanding of aggregate structures in aqueous solution may contribute to elucidation of the dynamic properties of bilayer-structures.

Aggregate structures of symmetric and asymmetric DAPs have been studied using SANS.[21] Electron microscope images of the microstructures formed by these systems have been obtained previously by negative staining transmission electron microscopy (TEM)[22] and freeze-fracture TEM.[23]

The effects of the n-alkyl chain length and asymmetry have also been investigated. The structure, phase transition temperature, and ion-induced vesicle fusion[22] have been researched, although work has been limited to symmetric or long-chain asymmetric molecules. All DAP samples with sufficiently long alkyl chains were found to form relatively stable vesicles, despite marked asymmetry in their chain length.[23]

In our previous study,[24] the short-chain effect on aggregate structures of the extremely asymmetric DAP anions, n-butyl(n-dodecyl)phosphate (BDoP) and n-hexyl(n-dodecyl)phosphate (HDoP), in water were studied by SANS, cryo-TEM, Raman scattering spectra, ^{13}C NMR, and selective nuclear Overhauser effect NOE(^{1}H{^{1}H}). The results showed that conformational change about the two P–O bonds in the DAP skeletons is related closely to variation in the shape of the aggregates. In particular, the length of the short-chain played an important role in the variation of shape.

For the asymmetric surfactant series of n-hexyl(n-decyl)-phosphate (HDeP), HDoP, and n-hexyl(n-cetyl)phosphate (HCeP), the extent of the molecular asymmetry increases with increasing length of the hydrocarbon chain. We may expect that spontaneous curvatures of aggregate systems formed by these surfactants play a critical role in their aggregation behavior and in the dynamics of their macroscopic or microscopic phase separation. However, the aggregate behavior of these extremely asymmetric surfactants remains unresolved.

The present study is focused on the effect of the long-chain on the self-organizing structures of such extremely asymmetric DAP anions in water. Fresh samples were aged for different periods of time, and their cryo-TEM images were examined. The time-dependent measurements have been discussed and have helped us understand the relationship between the molecular structures of DAPs and their dissipative structures. SANS and X-ray diffraction data were used to augment the cryo-TEM images.

■ MATERIALS AND METHODS

Materials. Extremely asymmetric di-n-alkylphosphates (DAPs)—(lithium n-hexyl(n-decyl)phosphate (HDeP), lithium n-hexyl(n-dodecyl)phosphate (HDoP), and sodium n-hexyl(n-cetyl)phosphate (HCeP)) (Scheme I)—were prepared as

Scheme I. Extremely Asymmetric Di-n-alkylphosphates (DAPs)
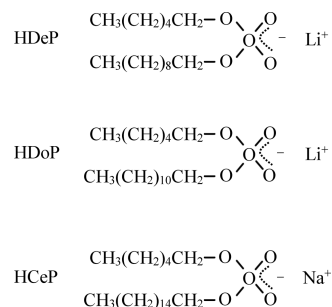
described previously.[25] Exhaustive extraction of unreacted n-alkylalcohols from the solid surfactants packed into a filter paper thimble in a Soxhlet extractor was carried out (solvent: benzene). Analysis of samples was made by ^{1}H and ^{13}C NMR and elemental analysis (C, H, and P). A minimum in the plots of equilibrium solution surface-tensions (γ_{eq}) against ln C (mol/L) was not found, confirming the high purity of the DAPs.

Phase Behavior Observations. Sample solutions were prepared by adding weighed amounts of DAP and water into glass ampules, which were then sealed and homogenized by heating and shaking. The thermotropic transition temperatures of the DAP-water systems were determined with a differential scanning calorimeter (Rigaku DSC 8230), scanned at a rate of 2 K/min by using a volatile pan with α−Al$_2$O$_3$ in the reference pan. The phase features of each sample were examined by visual inspection as it was held in a temperature-controlled water bath (rate of temperature elevation and cooling, 0.1 K/min).

Cmc Measurements. Electrical conductivity (κ, μS/cm) and ^{13}C NMR chemical shift (δ, ppm) methods were used to determine the critical micelle concentration (cmc). Electrical conductivity was measured with a TOA conductivity meter CG-

2A and a conductivity cell CG-7001PL (cell constant: 0.995 × 0.1) at 298 ± 0.01K.

The ^{13}C NMR spectra of the samples in D_2O (isotopic purity: 99.9%; in a 10 mm diameter sample tube) were recorded on a Bruker Avance-600 spectrometer, operated at 150 MHz (spectral width 238.3496 ppm, 65536 points in the time domain, acquisition time 0.9110004 s, and delay 6.00 μs) and locked on deuterium at 298 ± 0.1 K. The ^{13}C chemical shifts (δ_{obs}, ppm) were given relative to an external standard (1 M $(CH_3)_3Si-(CH_3)_3Na/D_2O$).

Preparation of Sample Solutions. The sample solutions for measurement of cryo-TEM were prepared by weighing the solid powder into a screw-top vial. The powder was dissolved to the desired concentration with doubly distilled water (Milli-Q, Millipore, 18.2 mS/m). Temperatures were chosen according to the phase diagrams in the isotropic micelle domain (asymmetric homologues were checked at 298 K). Temperatures were also taken above the phase transition temperature (chain melting) T_c, which indicates the transition from a frozen gel-like state to a fluid liquid crystalline state. The samples, which had been allowed to stand for up to 14 days or for two days were termed "aged samples" and "fresh samples", respectively.

Cryogenic-Temperature Ttransmission Electron Microscopy (cryo-TEM). Vitrified specimens for TEM were prepared in a controlled environment vitrification system (CEVS) at 298 K and 100% relative humidity, as previously described.[26] A droplet of the sample solution was placed in a lacy carbon film held with tweezers in the CEVS, blotted thin, and vitrified in liquid ethane at its freezing point. On-the-grid relaxation removed any flow-induced structures in the samples, and was performed by leaving the samples in the CEVS for 15−60 s after blotting and before vitrification. Vitrified samples were stored in liquid nitrogen (77 K), until viewing in the microscope. Specimens were transferred into a Philips CM120 microscope, operated at 120 kV, in an Oxford CT-3500 cooling holder, through its special purpose transfer station. After equilibration in the microscope at about 93 K, the specimen was examined in the low-dose imaging mode to minimize electron-beam radiation damage. The images were taken at a nominal under-focus of 41−43 nm, where any amplitude contrast is enhanced with phase contrast, and were recorded digitally by a Gatan 791 Multi-Scan CCD camera using the Digital Micrograph 3.1 software.

The cryo-TEM micrographs are two-dimensional projections of three-dimensional structures. A structure such as a vesicle gives high contrast around the edge, while a flat bilayer provides uniform contrast throughout.

X-ray Diffraction Measurements. Small-angle X-ray diffraction patterns of concentrated HDeP solutions were obtained using a RU-200 camera (Rigaku) with a three slit-system in the diffraction range of $1.2° < 2\theta < 10°$ at 298 K. Nickel-filtered Cu $K\alpha$ radiation (1.54Å) was used. The temperature of the sample was controlled by air within ± 1 K and measured with a digital thermometer (Sato-Keiryouki). The reciprocal spacing $s = 1/d = 2\sin\theta/\lambda$, where d, λ, and θ are the repeat distance, X-ray wavelength, and diffraction angle, respectively.

SANS Measurements and Analyses. The small-angle neutron-scattering (SANS) measurements were carried out at 298 ± 0.1 K using the SANS instrument (with quartz cell of 1 mm path length and with a sample-to-detector distance of 3 m) and the medium-angle neutron scattering instruments (WINK)

(with quartz cell of 2 mm path length) installed at the pulsed neutron source KENS (the National Laboratory for High Energy Physics, Tsukuba, Japan). The DAP samples in D_2O (belonging to an isotropic phase), which were allowed to stand for 7 days at 298 K after preparation, were placed in a quartz cell (path length: 1−2 mm). Smearing correction for each instrumental setting was also made using the instrumental resolution function approximated as a Gaussian function.

The scattering length density (ρ) of each component was calculated using the equation $\rho = \Sigma b_i/V$, where b_i is the scattering length of atom i, and V is the molecular volume.[27] The magnitude of the momentum transfer Q is given by $Q = (4\pi/\lambda)\sin(\theta/2)$, where λ is the incident wavelength (3−11 Å for SANS and 1−16 Å for WINK), and θ is the scattering angle. The intensity of the scattered neutrons was recorded on a position-sensitive 2D detector.

The scattering intensity coming from the sample solution was corrected for the detector background and sensitivity, empty cell scattering, incoherent scattering, and sample transmission. The intensity spectrum of the sample solution below the cmc was subtracted from that of the sample solution above the cmc. The intensities thus corrected were then azimuthally averaged to give values of the relative scattering intensities vs Q. Normalization of the observed data to an absolute intensity scale was made by using the scattering spectrum and transmission of a 1 mm water sample for SANS and WINK.

The neutron-scattering intensity $d\Sigma(Q)/d\Omega$, depending on the magnitude of a scattering vector (Q), can be expressed as a function of the particle structure factor $P(Q)$ and the size and orientation weighted interparticle structure factor $S'(Q)$,

$$d\Sigma(Q)/d\Omega = I_0 P(Q)S'(Q) \tag{1}$$

where I_0 is the extrapolated zero-angle scattering intensity independent of the micellar shape and is a function of the number-average aggregation number n. I_0 is given by eq 2 in terms of the volumes of the micelle core (V_c, in Å^3) and overall micelle (V_m, in Å^3) and the average neutron-scattering length densities of the polar shell, hydrophobic core, and solvent (ρ_p, ρ_c, and ρ_s, in Å^{-2}, respectively).

$$I_0 = \{(C - cmc)N_A/1000n\}10^{-16}$$
$$[(\rho_p - \rho_c)V_c + (\rho_s - \rho_p)V_m]^2 \tag{2}$$

where N_A is Avogadro's number, C is the concentration of surfactant in mol dm^{-3}, and cmc denotes the critical micelle concentration. $P(Q)$ for an ellipsoidal particle is given by the following form,

$$P(Q) = \int_0^1 |F(Q, \mu)|^2 d\mu \tag{3}$$

$$F(Q, \mu) = x((3(\sin(QR_1) - QR_1\cos(QR_1))/(QR_1)^3)$$
$$+ (1 - x)((3(\sin(QR_2) - QR_2\cos(QR_2))/(QR_2)^3) \tag{4}$$

$$x = ((\rho_p - \rho_c)V_c)/((\rho_p - \rho_c)V_c + (\rho_s - \rho_p)V_m) \tag{5}$$

R_1 and R_2 for the prolate model are given by

$$R_1 = [a^2\mu^2 + b^2(1 - \mu^2)]^{1/2} \tag{6}$$

$$R_2 = [(a + t)^2\mu^2 + (b + t)^2(1 - \mu^2)]^{1/2} \tag{7}$$

and R_1 and R_2 for the oblate model

$$R_1 = [a^2(1 - \mu^2) + b^2\mu^2]^{1/2} \tag{8}$$

$$R_2 = [(a + t)^2(1 - \mu^2) + (b + t)^2\mu^2]^{1/2} \tag{9}$$

where a and b are the major and minor axes of a micellar particle, respectively, t is the thickness of the polar core of a micellar particle, and μ is the cosine of the angle between the direction of the minor axis b and the scattering vector Q.

The size and orientation weighted interparticle structure factor $S'(Q)$ can be calculated approximately by the following equation

$$S'(Q) = 1 + \beta(Q, \mu)[S(Q) - 1] \tag{10}$$

$$\beta(Q, \mu) = |\langle F(Q, \mu)\rangle^2|/\langle|F(Q, \mu)|^2\rangle \tag{11}$$

where $S(Q)$ is the interparticle structure factor.[28]

When the micellar model for $P(Q)$ translates into the model for $S(Q)$, the micelle was assumed to be a rigid charged sphere of diameter σ, interacting through a dimensionless screened Coulombic potential.

$S(Q)$ for a one-component macro-fluid was calculated using Hayter and Penford's[29] and Kotlarchyk and Chen's treatments (K-C treatment I).[30] In the K-C treatment I, one may approximate the micelle core as a rigid sphere, provided that the shape of the ionic micelle is ellipsoidal with an axis ratio (a/b) no greater than 2. For systems with an a/b ratio greater than 2, Kotlarchyk and Chen[30] proposed another approach with a more accurate prescription of the micelle diameter, in which orientational averaging of particles affects $S'(Q)$ (K-C treatment II).

In the K-C treatment II, the macro-ion diameter (σ) for the calculation of $S'(Q)$ is given by eq 12,

$$\sigma = [2(f + 1)(a + t)(b + t)^2]^{1/3} \tag{12}$$

where

$$f = 3/4[1 + (\sin^{-1} P)/\{P(1 - P^2)^{1/2}\}][1 + \{(1 - P^2)/2P\}$$
$$\ln((1 + P)/(1 - P))] \tag{13}$$

$$P = [\{(a + t)^2 - (b + t)^2\}/(a + t)^2]^{1/2} \tag{14}$$

The observed SANS intensity data of the DAP aggregate systems were analyzed with the number-average aggregation number (n), degree of ionization of a macro-ion (α), and the number of hydrated-CH_2 groups (n_{wt}) as fitting parameters, as described in the literature.[28] The Stern layer of thickness t consists of the head groups, associated with counter-ions and water molecules, and hydrated-CH_2 groups. The values of a, b, and t were calculated using the extracted values of n_{wt} and n. The average hydration number N_s per surfactant polar head was calculated by the equation $N_s = \{V_p - n(V_{head} + r_c(1 - \alpha)V_{ion})/ nV_{solvent}$, where V_{head}, V_{ion}, V_p, and $V_{solvent}$ are the volumes of the polar head in the Stern layer per surfactant molecule (excluding the counterion), of a counterion, of the polar shell, and of a water molecule, respectively, and r_c is the number ratio of [counterion]/[surfactant molecule].

RESULTS AND DISCUSSION

The phase behavior of the DAP-water systems was examined by visual inspection and differential scanning calorimetry. The phase maps of the two DAP binary systems consisted mainly of a homogeneous and transparent isotropic phase, a lyotropic liquid crystalline phase, and a coagel phase (phase maps not shown). The phase feature was also confirmed under a

polarizing microscope. The isotropic phase and the liquid crystalline phase were below 0.90 mol/l and between 0.90−2.40 mol/l, respectively, for HDeP; below 1.0 mol/l and between 1.0−3.0 mol/l, respectively, for HDoP; and below 0.38 mol/l and between 0.38−0.75 mol/l, respectively, for HCeP.

For the isotropic solutions of HDeP and HCeP, the cmc values were determined from plots of specific electrical conductivity, κ, against concentration (C, mol/l). In the κ-C plots for HDeP, two inflection points at lower and higher concentrations were observed and were regarded as the first and second cmc, respectively: for HDeP, 3.30×10^{-3} and 2.60×10^{-2} mol/l (298 K); for HCeP, the first cmc (3.70×10^{-4} mol/l) was determined from the κ-C plots (298 K) and the second cmc (2.20×10^{-3} mol/l) was obtained by NMR (323 K).

For HDoP, the first and second cmcs (1.2×10^{-3} and 3.7×10^{-2} mol/l, respectively) were cited from our previous paper.[24]

Cryo-TEM of Aged HDeP, HDoP, and HCeP Samples. Cryo-TEM images which show the effect of short chains on aggregate structures of BDoP and HDoP have been reported previously.[24] For the cryo-TEM images of HDoP at concentrations above the first cmc (1.20×10^{-3} mol/l), results of special relevance to this present study may be summarized as follows.

For the sample solution at the lowest concentration (2.8×10^{-2} mol/l), the main aggregates were spheroidal micelles. At a concentration (4.50×10^{-2} mol/l) above the second cmc, the network-like structures of flexible thread-like micelles (TLMs) appeared among the predominant spheroidal micelles. At a higher concentration (7.40×10^{-2} mol/l), a few unilamellar vesicles and TLMs were found on the background of spheroidal micelles. As the concentration was increased further, the proportion of long, flexible TLMs increased while that of spheroidal micelles decreased. At the highest concentration imaged (9.87×10^{-2} mol/l), TLMs and a few spheroidal micelles were seen, in addition to uni- and multilamellar vesicles and stiff ribbon-like aggregates (RLAs). Highly ordered stiff RLAs, forming microsolid phase domains, began appearing at this concentration, implying a transition from TLMs to RLAs (TLM → RLA transition).

X-ray diffraction patterns of the concentrated HDoP aqueous samples were examined[31] for further understanding of the cryo-TEM images of the dilute samples. The results indicated the existence of a lamellar phase at concentrations of 0.7−2.2 mol/l, caused by further growth of such highly organized RLAs. Thus, the RLA-structures observed in the cryo-TEM images of HDoP[24] were regarded as a lamellar phase coexisting with a spheroidal micellar-phase. This concept may be applied to the RLA structures in the images of HDeP and HCeP, since the X-ray diffraction patterns of their concentrated aqueous samples provided evidence of the lamellar phases (discussed below).

In the present study, cryo-TEM observations of aged samples of HDeP and HCeP were also carried out (298 K), in order to examine the long-chain effect on the aggregational behavior for the series HDeP, HDoP, and HCeP. The reproducibility of these cryo-TEM images was confirmed by repeated measurements

Concentration-dependent images similar to those of HDoP were also seen on a background of spheroidal micelles. As the concentrations were increased, the microstructures were transformed into more elongated lower-curvature structures. As the asymmetry in the molecule increased, lower curvature structures, such as TLMs and vesicles, appeared even at low
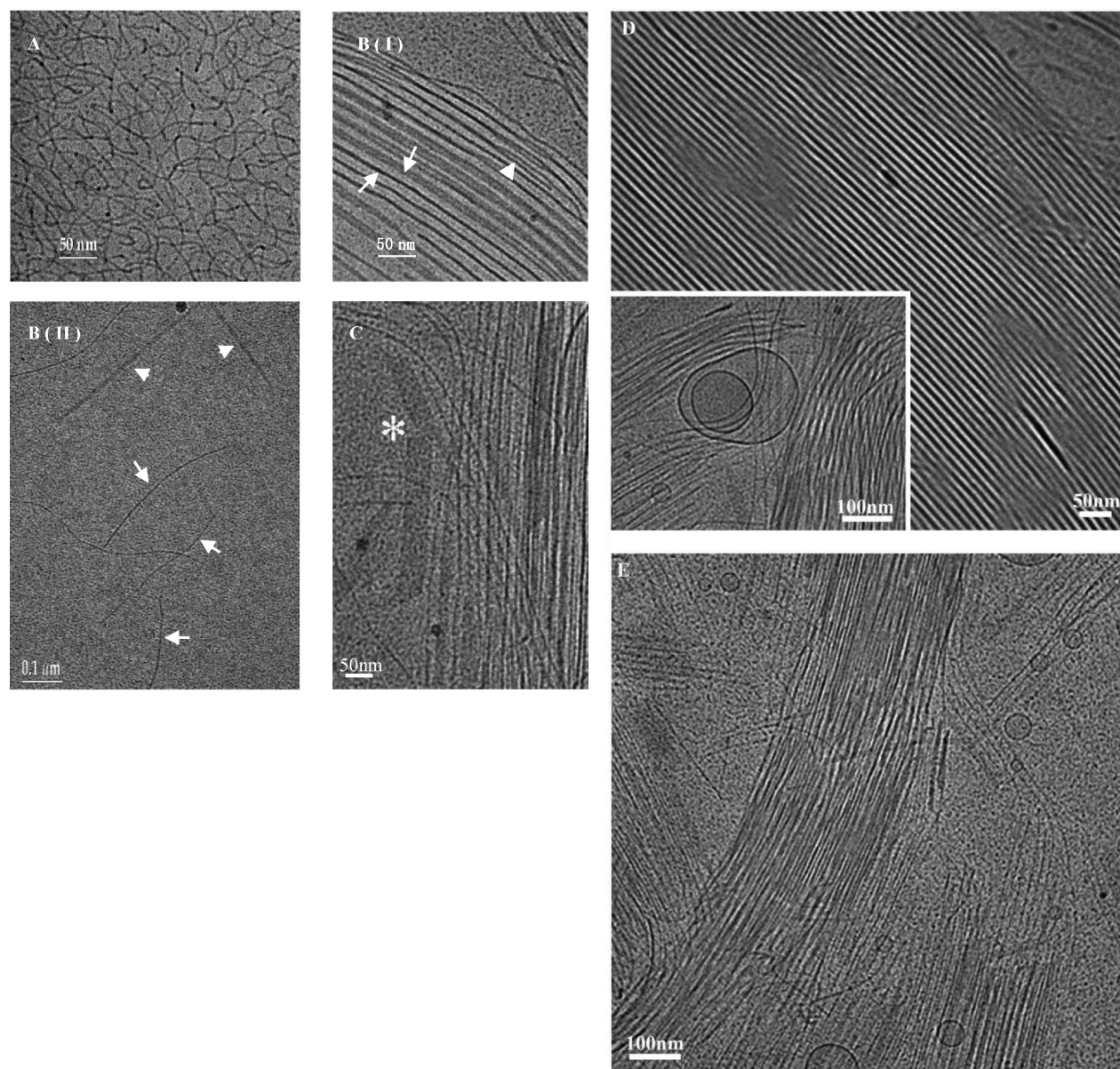
Figure 1. Representative cryo-TEM images of the aged HDeP samples prepared at 298 K: networks of very long, flexible TLMs at 1.50×10^{-2} mol/l (A); ordered alignment of thin, slender RLAs (arrows) consisting of extended TLMs (arrowhead) (B(I)); fragments of TLM (arrows) and thin, slender RLAs (arrowheads) (B(II)); ordered alignment of extended TLMs and short, thin, stiff RLAs (asterisk) at 6.70×10^{-2} mol/l (C); highly ordered structures coexisting with spheroidal micelles and vesicles (the inset shows other prevalent structures) at 7.40×10^{-2} mol/l (D); ordered structures coexisting with spheroids and unilamellar vesicles at 10.24×10^{-2} mol/l (E).

concentrations. Noteworthy characteristics of the images of HDeP and HCeP are described as follows.

For the aged HDeP sample up to 4.6×10^{-2} mol/l (and above the second cmc), the networks of very long, flexible TLMs were found on a background of numerous spheroidal micelles (Figure 1A). At a higher concentration (6.70×10^{-2} mol/l), RLA structures with low electron density (i.e., thin) and some ordered structures appeared (Figure 1B(I) and C). The ordered RLA structures seem to be made up of ribbon-like and thread-like structures packed tightly (Figure 1B(I), arrowhead). These two structures seem to be the same, but at different

inclinations with respect to the electron beam. The apparent dark threads are flat ribbons seen edge-on, and the apparent ribbons are seen face-on (arrows). Moreover (Figure 1B(II)), relatively long fragments (arrows) of TLMs were also found together with the fragments of thin, slender RLAs (arrowheads). Stiff, flat bilayers similar to wider ribbons were also seen (Figure 1C, asterisk). Thin, slender RLAs were aligned in an orderly fashion with approximately constant spacing (11−12 nm).

In the images of the aged HDeP sample (7.44×10^{-2} mol/l), ordered structures and stiff RLAs were more abundant and a
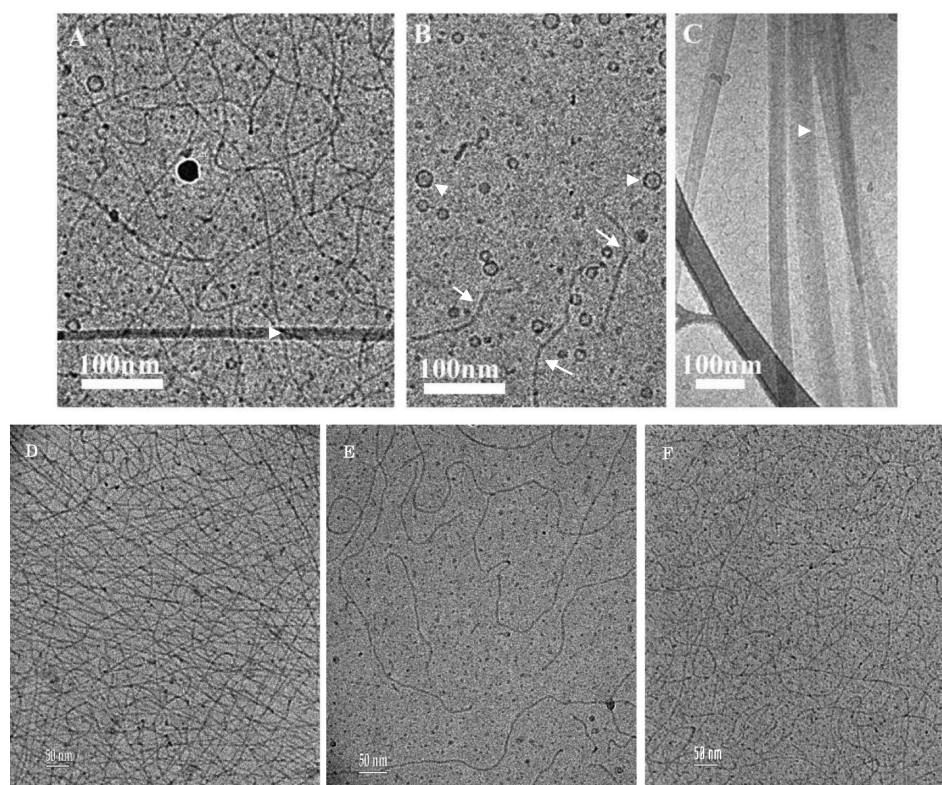
Figure 2. Representative cryo-TEM images of the HCeP samples prepared at 298 K: long, flexible TLMs and long thin, stiff RLA (arrowhead) against a background of spheroids (A); fragments of flexible TLM (arrows) and unilamellar vesicles (arrowheads) (B); long, wide, stiff RLAs (arrowhead) (C); networks of long, flexible, or extended TLMs (D); fragments of flexible TLMs at 1.20×10^{-2} mol/l (E); networks of very long, flexible TLMs at 2.34×10^{-2} mol/l (F).

few vesicles also appeared (Figure 1D). Ordered structures and stiff, flat RLAs at this concentration were much more densely packed than were the thin RLAs in the 6.7×10^{-2} mol/l solution. The stiff RLAs in these images provided very high mass-thickness image contrast (Figure 1D). The thread-like structures exhibited much less contrast relative to the vitreous ice matrix, indicating that these highly ordered structures are in fact dense assemblies of stiff, flat RLAs seen edge on, thus explaining the high mass-thickness contrast.

As for the double-shell vesicle in the image of the aged HDeP sample (7.44×10^{-2} mo/l) (Figure 1D, inset), the outer shell with various curvatures was highly deformed and was faceted (polyhedral), although the shape of the inner shell was close to spherical. The polyhedral structure observed here is unlike those which are present in the gel phase of double-chained lipids in water.[32] The latter occur at temperatures below the lipid chain-melting temperature (T_c) and are characterized by polyhedral, ripple-edged vesicles. The presence of a faceted shell in this present system is of a different origin, because the temperature was above the T_c. Similar structures formed above T_c were seen previously,[33] but no satisfactory explanation for the angularities has been found.

Since the shape of a vesicle depends strongly upon the osmotic pressure difference between the outer inside media,[34] the osmotic pressure effect should contribute to deformation of the outer shell. However, the faceted structure of the HDeP vesicle may be ascribed to stabilization of a specific conformation[24] about the two P−O bonds of the DAP skeletons in the lamellar shell rather than the osmotic pressure effect.

At a higher concentration (10.24×10^{-2} mol/l) (Figure 1E), the highly ordered stiff RLAs became more numerous and dense, and were observed on the background of spheroidal micelles; small unilamellar vesicles with high curvatures were also seen. Typical structures of "loose" RLAs coexisted with spheroidal micelles and vesicles at this concentration (Figure 1E). The loose RLAs, which had already appeared at about 6.70×10^{-2} mol/l, became very dense and ordered at higher concentrations. Furthermore, ribbon-like and thread-like structures were also aligned in an orderly fashion toward different directions. The loose structures may manifest some distortion or irregularities in the RLA-structures or the transient intermediates on the way to the final highly ordered stiff RLAs.

Thin, slender RLAs, loose RLAs, and highly ordered stiff RLAs imaged on the background of spheroidal micelles were also ascribed to a microsolid lamellar phase formed by HDeP,[31] regarded as a dissipative system far from equilibrium.

For the two aged HCeP samples (1.17×10^{-2} and 2.34×10^{-2} mol/l), various aggregate structures coexisted in the background of spheroidal micelles. Typical microstructures are shown in Figure 2.

The network structures of very long, flexible TLMs were formed at concentrations as low as 1.17×10^{-2} mol/l (Figure 2A). Unilamellar vesicles with various sizes (arrowheads) were found together with the fragments of flexible TLMs (arrows) (Figure 2B). Very long, thin, stiff RLAs (asterisk) were also seen (Figure 2A and C), as well as networks consisting of very long, flexible TLMs and very long, extended TLMs (Figure 2D). Indeed, all of TLM-networks, TLM-fragments of various sizes, small unilamellar vesicles, and stiff RLAs were seen even at a low concentration.

At a higher concentration (1.20×10^{-2} and 2.34×10^{-2} mol/l), the networks of very long TLMs disappeared and only some of the relatively short, flexible TLMs and their fragments (Figure 2E) and fewer long TLMs (2F) remained amidst a background of spheroidal micelles. This result may be regarded as evidence that breaking of the very long, flexible TLMs occurred at higher concentration (TLM-breakage). Above the concentration 2.34×10^{-2} mol/l, the HCeP-solutions were in a very viscous gel-state at room temperature. Since this gel-state persisted even at 337 K, no cryo-TEM investigation was carried out. Thus, various shapes of RLAs, from thin, long, and flexible to wider and stiffer, were a preferred structure for these asymmetric DAP species.

HDeP is more likely to adopt a highly ordered RLA in water, compared with HDoP and HCeP. This structure may come from the difference in the main hydrocarbon chain length, since the shorter *n*-decyl chain conforms easily to an ordered structure upon aggregation.[24]

Time-Dependent Cryo-TEM Images of Fresh Samples and the Aging Effect. To assist understanding of the concentration-dependence of the complex, dynamic behavior of asymmetric DAP aggregates, the effect of aging on the sample solution was examined by leaving the fresh HCeP solution (2.34×10^{-2} mol/l) for different times (at 298 K) before the cryo-TEM observation.

The time-dependent cryo-TEM images are shown in Figure 3. When this sample was aged for 48 h either without relaxation or with relaxation (for 20 s on the grid), very long, flexible TLMs became predominant and provided the network structures (Figure 3A). After aging for one week, many of the very long, flexible TLMs disappeared and relatively shorter, flexible TLMs and their fragments appeared against a background of spheroids (TLM-breakage) (Figure 3B). That

is, the breakage of a TLM should be assigned to a structural-transition from very long TLM micelles to shorter TLMs or smaller micelles. Shorter, flexible TLMs and fragments which have newly appeared may be regarded as the products of this breakage. Some very long TLMs were also imaged together with shorter fragments, possibly implying that the structural-transition had not attained the final state but was still progressing.

For the same sample aged for two weeks, giant, stiff RLAs (Figure 3C(I)) were seen together with a few unilamellar vesicles (Figure 3C(II)), showing that the giant stiff RLAs were formed spontaneously and slowly from TLMs, TLM-fragments, and spheroidal micelles (TLM→RLA transition). The stabilized giant, stiff RLAs were found to separate very slowly as a microsolid lamellar phase (RLAs phase separation) along with spheroidal micelles, also indicating that this system is far from equilibrium.

Time-dependent cryo-TEM images were collected from fresh and aged HDeP samples at high concentration (10.24×10^{-2} mol/l) at 298 K (Figure 4), to follow the process of formation of the highly ordered stiff RLAs. Repeated measurements were carried out to confirm the reproducibility of these images.

In the image taken from a cryo-TEM specimen prepared after 24 h aging (298K) (Figure 4A), we see uni- and multilamellar vesicles with various sizes together with a very large disk-like structure (arrowhead; note, no dark edge), a very large unilamellar vesicle (V), short RLAs (arrow), and thin, slender RLAs (asterisk). A number of long, slender RLAs, in addition to short, slender RLAs, aligned at a constant spacing (*ca* 13 nm) (ordered alignment of RLAs) are also seen.

In particular, it should be noted that the very large unilamellar vesicle was faceted (Figure 4A, V). The unilamellar vesicles with intermediate sizes were observed to be deformed shapes with various axis ratios deviating from unity, indicating that such lamellar layers may be liquid-like and easily deformed. For multilamellar vesicles, the outer shell was markedly deformed, compared with the inner shell. The great variety of deformations of these vesicles was due to structural variation of the lamellar layers responding to dynamic pressure and shear arising from the water-flow during specimen preparation (discussed later), although a contribution from the effect of osmotic pressure may also be present.

In the cryo-TEM images obtained immediately after 24 h aging, the network structures of long, flexible TLMs were not observed, possibly indicating that formation and breaking of the networks occurred rapidly within 24 h at high concentrations.

In the images from specimens prepared after 48 h, the vesicular-structures practically disappeared, and the ordered alignment of thin, slender, and extended RLAs with various lengths became predominant (Figure 4B). This phenomenon must be a phase-transition from the vesicles to thin, slender RLA structures (vesicle → RLA transition). Each of RLAs was found to consist of shorter, extended TLMs (Figure 4B, arrows). The prevalent appearance of thin, slender RLAs consisting of extended TLMs was also confirmed in the sample aged for one week (Figure 4C(I) and C(II), arrows).

For the same sample aged for two weeks, most of these RLAs (asterisk) disappeared and uni- and multilamellar vesicles with various sizes (arrowhead) again became abundant on the background of spheroidal micelles (Figure 4D), implying a spontaneous, very slow transition from the RLA phase to the vesicle phase (RLA → vesicle transition).
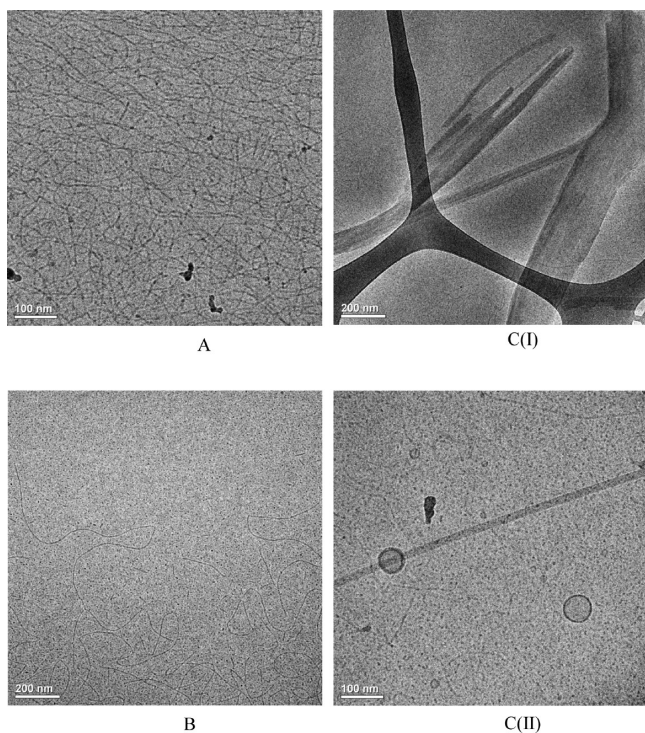

Figure 3. Representative time-dependent cryo-TEM images of the HCeP sample (2.34×10^{-2} mol/l, 298 K) at different aging times: (A) 48 h, (B) 1 week, C(I) and C(II) 2 weeks.
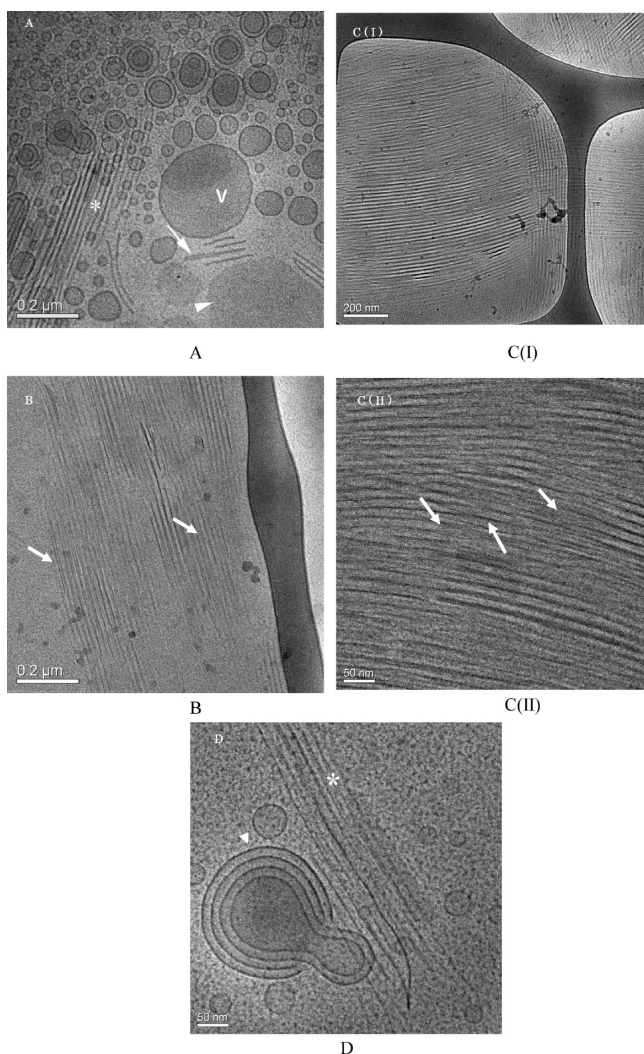
Figure 4. Representative time-dependent cryo-TEM images of the HDeP sample (10.24×10^{-2} mol/l, 298 K) at different aging times: (A) 24 h; a giant disk (arrowhead), a very large vesicle (V), short RLAs (arrow), and orderly aligned long RLAs (asterisk); (B) 48 h; ordered RLAs consisting of extended TLMs (arrows); (C) 1 week, orderly aligned RLAs (C(I) and C(II)) consisting of extended TLMs (C(II), arrows); (D) 2 weeks, uni and multilamellar vesicles (arrowhead) and thin slender RLAs (asterisk).

We note the presence of a large vesicle with four shells (average separation between shells: *ca* 13 nm; Figure 4D), in which the two outside lamellar shells were broken and the two inside shells, with a tongue-like shape, were emerging out of the broken outer shells. The eccentric image provides direct evidence for breaking of a multilamellar vesicle, which may be due to the osmotic pressure difference effect,[34] implying that breaking of vesicles may occur in the course of vesicle-RLA reversible transition.

SANS of Aged Samples. In our previous paper,[24] the short-chain effect on aggregate structures of BDoP and HDoP was reported on the basis of results of cryo-TEM, SANS, Raman scattering, ^{13}C NMR, and selective NOE studies. Cryo-TEM provided direct images to support the average aggregation size and shape predicted by the SANS analyses with use of $P(Q)$ for a biaxial prolate-spheroidal model.

In this present study, the concentration-dependence of the number-average aggregation number for HDeP and HCeP in water was also examined by SANS, in order to understand the effect of the long chain on the cryo-TEM images of the series HDeP, HDoP, and HCeP.

The SANS spectra observed for HDeP and HCeP have also been analyzed using the $P(Q)$ model[35] used for the SANS analyses of BDoP and HDoP,[24] in order to compare the concentration-dependence of the number-average aggregation number for HDeP, HDoP, and HCeP. It is emphasized that the same theoretical model has been used so as to ensure validity of the comparison.

In the cryo-TEM images at low concentrations of the present extremely asymmetric DAP solutions, variable micelle shapes containing nonpredominant and unhomogeneous aggregates were readily observed, probably occurring from their molecular asymmetry causing instability of their shape. Therefore, in this present SANS study, a biaxial prolate-spheroidal model in monodispersed states was used to examine the concentration-dependence of number-average aggregation-numbers.

Of the three methods (Hayter and Penford's treatment,[29] K-C treatments[30] I and II) used to calculate the interparticle structure factor, the K-C treatment II[30] provided a better fit to the observed intensity data.

The uncertainty in SANS intensity is dominated by simple counting statistics in the signal. The total number of counts for each sample was varied, according to the concentration of the DAP samples, so as to minimize error bars in the intensity. For HDoP and HCeP, the size of error bar (the percent uncertainty) was $1-1.3\%$ ($\pm$) of the observed intensity at each datum point (q range: $1.5 \times 10^{-2} < q(\text{Å}^{-1}) < 0.300$). For HDeP, the sizes of error bars were $0.3 - 1.0\%$ ($\pm$) ($1.5 \times 10^{-2} < q(\text{Å}^{-1}) < 0.170$), $1-1.3\%$ ($\pm$) ($0.170 < q(\text{Å}^{-1}) < 0.240$), and $1.4-1.6\%$ ($\pm$) ($0.240 < q(\text{Å}^{-1}) < 0.290$). Representative error bars in the observed SANS intensities are shown in the lnI(q) − lnq plots of HDeP (Figure 5A).

The observed SANS spectra and calculated spectra of aged HCeP samples, as representatives, are shown in Figure 5B. Broad peaks indicate the presence of interaggregate interactions in these sample systems. The interaction peaks increased markedly in intensity in region III′ (Figure 5B (a, b, and c)), possibly due to enhanced interactions with the increased population of RLAs or to variation in shape of a TLM.

The quality of fit between the observed and calculated data points was judged by χ^2, which is defined as $\chi^2 = \Sigma_{iN} (I_{calc}(Q_i) - I_{obs}(Q_i))/I_{obs}(Q_i))^2]/(N - p)$, where $I_{obs}(Q_i)$ and $I_{calc}(Q_i)$ denote the observed and calculated scattering intensities, respectively. N is the total number of data points, p the number of parameters to minimize χ^2 which are variable, and Σ_{iN} denotes the summation from the data point 1 to N.[36] The values of χ as an indicator for the quality of fit for HCeP are shown in the legend for Figure 5. The average values of χ for HDeP and HDoP were within the range $1.3-3.0$.

The SANS analyses, based on the biaxial prolate-spheroidal model, provided the values for the degree of ionization of a micelle (α), n, the number of hydrated-CH_2 groups (n_{wt}), and the average hydration number (N_s) per surfactant polar head, and are listed in Table 1A and B.

Figure 6 shows the number-average aggregation number n values of an aggregate as a function of the square root ($X - X_{cmc})^{1/2}$ of the monomer concentration (X: molar fraction),[37] attributable to formation of the aggregates.

We should note that there are two inflection points in the plot of n against ($X - X_{cmc})^{1/2}$ for the two sample systems (Figure 6). For HDeP, the first inflection point (2.43×10^{-2}
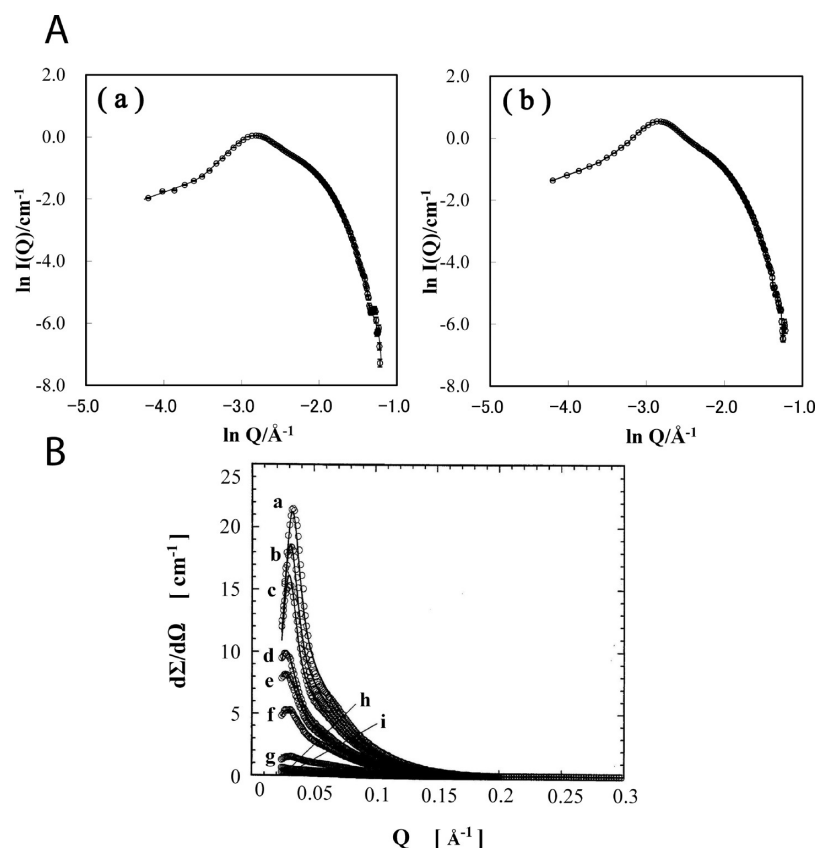
Figure 5. (A) The ln I(q)/cm^{-1} − ln q/Å^{-1} plots with error bars for the observed SANS spectra of HDeP ((a) 5.40×10^{-2} mol/l (the network-like structures of flexible TLMs are predominant at this concentration); (b) 7.4×10^{-2} mol/l (stiff RLAs are abundant at this concentration)).The solid lines indicate the best fit curves calculated. (B) Observed SANS spectra (filled circles) of HCeP in D$_2$O (a, 7.00×10^{-2} mol/L; b, 5.9×10^{-2} mol/L; c, 4.68×10^{-2} mol/L; d, 3.51×10^{-2} mol/L; e, 3.04×10^{-2} mol/L; f, 2.34×10^{-2} mol/L; g, 1.20×10^{-2} mol/L; h, 4.7×10^{-2} mol/L; i, 2.30×10^{-2} mol/L) and best-fitted scattering intensity profiles (solid lines). The agreement (χ) between experimental and calculated intensities is 2.3 for (a), 2.0 for (b), 2.3 for (c), 2.2 for (d), 2.5 for (e), 2.0 for (f), 2.1 for (g), 2.2 for (h), and 2.1 for (i). Error bars (1−1.3% of observed intensity) are not shown since they would be encompassed within the size of the symbols.

mol/l), very close to the second cmc (2.60×10^{-2} mol/l) determined by specific electrical conductivity, can be regarded as the second cmc determined by SANS. The second inflection point (5.40×10^{-2} mol/l) was not found by surface tension, electrical conductivity or NMR. Thus, this point can be regarded as the third cmc (Figure 6A), determined by SANS. In the plot for HCeP, two inflection points appeared at 1.94×10^{-2} and 5.27×10^{-2} mol/l (Figure 6B). Since the first inflection point corresponds approximately to the second cmc (2.20×10^{-2} mol/l) determined by NMR, this concentration (1.94×10^{-2} mol/l) is assigned to the second cmc for HCeP. The second inflection point at 5.27×10^{-2} mol/l, which was not obtained by the other methods, can be regarded as the third cmc determined by SANS. In these plots, the concentration regions below the second cmc, between the second and third cmcs, and above the third cmc are termed regions I, II, and III, respectively, for HDeP (Figure 6A) and regions I′, II′, and III′, respectively, for HCeP (Figure 6B).

The plot for HDoP, which was reported in a previous paper,[24] also provided two straight lines crossing at a concentration (3.90×10^{-2} mol/l) very close to the second cmc, indicating that the growth of TLMs increases markedly above this concentration, estimated from the concentration-dependence of the cryo-TEM images. Thus, for HDoP the regions below and above the second cmc are termed regions I and II, respectively.

The values of n, n_{wt}, and axis ratio obtained by the SANS analyses were connected with the concentration-dependence of the cryo-TEM images for DAPs.

For HDeP and HCeP, as well as for HDoP, the number-average aggregation number (n) increased with increasing micelle-concentration below the second cmc, reflecting the growth of spheroidal micelles occurring in this region. Extrapolation of the straight line in the same region provided the number-average aggregation number, n_0, of a minimal micelle at the first cmc: 23 for HDeP and 90 for HCeP. The axis ratios of the minimal micelles were 1.7 for HDeP and 1.6 for HCeP, indicating a spheroidal shape for these minimal micelles. For HDoP,[24] the n_0 value and axis ratio were 27 and 1.0, respectively.

For HDeP, the number-average aggregation number, n, increased from 37 to 45 in region II and from 45 to 68 in region III, reflecting the growth of TLMs and RLAs, respectively, against a background of spheroidal micelles. The slope in region III was greater than that in region II, reflecting the rapid increase in growth of highly ordered RLAs, as imaged by cryo-TEM. For HDoP,[24] the increase of n from 109 to 220 in region II, also reflects the growth of TLMs.

For HCeP, variation of the n value from 207 to 370 in region II′ reflects the elongation process of TLMs, and the increase of n in region III′ contains the greater contribution of highly ordered RLAs.

Table 1. Parameters Extracted from SANS Analyses of the HDeP (A) and HCeP (B) Micellar Systems[a]

C (mol/l)	n	α	n_{wt}	a (Å)	b (Å)	t (Å)	$(a+t)/(b+t)$	N_s
(A)								
(a) 1.50×10^{-2}	29.2 (0.51)	0.32	4.2	21.00	8.93	9.35	1.66	32
(b) 2.00×10^{-2}	29.4 (0.42)	0.35	4.5	21.50	8.40	9.61	1.73	34
(c) 2.40×10^{-2}	30.0 (0.43)	0.41	4.4	22.50	8.62	9.72	1.76	32
(d) 3.10×10^{-2}	32.1 (0.44)	0.39	4.6	24.23	8.50	9.87	1.78	32
(e) 3.30×10^{-2}	37.2 (0.40)	0.43	4.3	27.51	8.79	9.60	1.97	29
(f) 4.60×10^{-2}	41.0 (0.41)	0.40	4.4	30.73	8.62	9.73	2.14	28
(g) 5.40×10^{-2}	45.4 (0.41)	0.37	4.9	34.82	8.00	10.30	2.34	29
(h) 6.03×10^{-2}	53.3 (0.50)	0.32	4.9	40.33	8.04	10.34	2.75	27
(i) 6.59×10^{-2}	60.2 (0.47)	0.31	5.1	45.53	7.74	10.60	3.06	26
(j) 7.42×10^{-2}	68.4 (0.44)	0.28	5.6	50.10	7.13	11.21	3.12	25
(B)								
(a) 2.30×10^{-3}	105.5 (0.46)	0.17	3.4	37.69	17.38	8.60	1.78	18
(b) 4.70×10^{-3}	103.3 (0.41)	0.20	2.6	35.20	18.40	8.60	1.62	15
(c) 1.20×10^{-2}	113.2 (0.42)	0.15	3.2	38.18	18.30	7.60	1.76	13
(d) 2.34×10^{-2}	207.0 (0.45)	0.10	3.3	73.63	17.63	8.29	3.16	14
(e) 3.04×10^{-2}	306.3 (0.40)	0.05	4.0	110.50	16.74	9.18	4.26	14
(f) 3.51×10^{-2}	354.0 (0.42)	0.06	3.9	127.50	16.87	9.05	5.57	13
(g) 4.68×10^{-2}	370.3 (0.43)	0.09	1.6	126.20	19.79	6.13	5.11	10
(h) 5.90×10^{-2}	409.5 (0.40)	0.09	0.8	136.40	20.80	5.12	5.46	9
(i) 7.00×10^{-2}	415.9 (0.45)	0.09	0.5	137.40	21.19	4.74	5.48	9

[a] n, the average aggregation number (the associated error is in parentheses); α, the degree of ionization of a micelle; n_{wt}, the number of hydrated methylene groups; a and b, the major and minor axes of a prolate micelle; t, the thickness of the Stern layer; N_s, the average hydration number per surfactant polar head in the micelle.
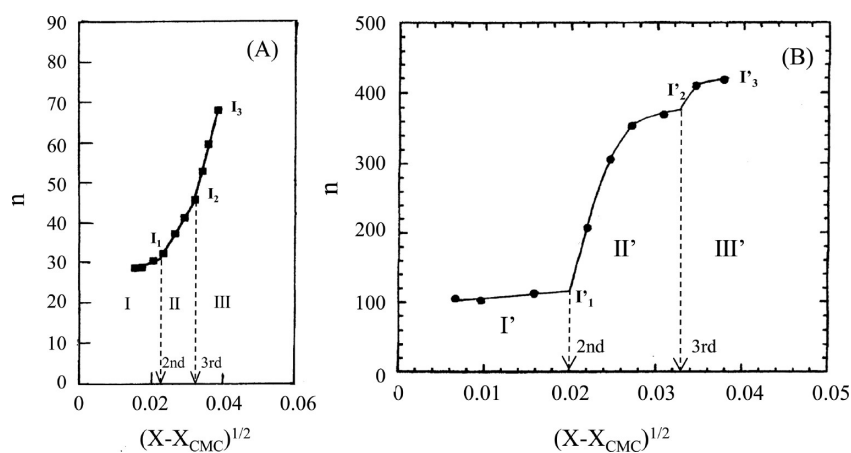

Figure 6. Plot of n as a function of $(X - X_{cmc})^{1/2}$ in the DAP-D$_2$O systems (HDeP (A) and HCeP (B)) ("2nd" denotes the second cmc, and "3rd" the third cmc).

Thus, the n values in the region II (or II′) for HDeP, HDoP,[24] and HCeP tend to increase in the order HDeP < HDoP < HCeP, showing that the average length of a TLM formed by each of the DAPs also increases in that order.

The axis ratio for HDeP was found to increase rapidly in region III, indicating marked variation in the average shape of these micelles. The abundance of giant, stiff RLAs in this region would cause a further increase in the axis ratio.

For HCeP, a rapid increase in axis ratio in region II′ (Table 1B) should be due to the predominant TLMs and their growth process, and that in region III′ to the contribution of stiff, wide RLAs.

We should note the variation in the number (n_{wt}) of hydrated-CH$_2$ groups for the decyl chain of HDeP and for the cetyl chain of HCeP, as predicted by the SANS analyses (Table 1). For HDeP, the n_{wt} value tends to increase above the third cmc, while for HCeP the n_{wt} value decreases markedly above

this concentration. This difference possibly results in the difference in the extent of hydration of the RLA structures of HDeP and HCeP.

When we compare the average values of n_{wt} and N_s among HDeP, HDoP,[24] and HCeP, they tend to decrease in the order HDeP > HDoP > HCeP, indicating that the extent of hydration of the polar region in their aggregates becomes smaller, depending strongly upon the length of the main hydrocarbon chain.

Origin of TLM- or RLA-Breakage and the Role of a Limiting Size. The cause of TLM-breakage, seen in the images of asymmetric DAP surfactants, may be explained as follows, on the basis of the one-dimensional aggregate theory.[38]

In the one-dimensional model,[38] we define the bond energy between unit-monomers in the aggregate, relative to isolated unit-monomers in solution, as equal to $\alpha \kappa T$ (α is an arbitrary

positive number, κ the Boltzmann constant, and T the absolute temperature).

The density distribution function (D_i) of molecules in aggregates consisting of i molecules is given by

$$D_i = i(1 - (1/(fe^{\alpha})^{1/2})^i e^{-\alpha}/f \qquad (15)$$

where f is the molar fraction of the solute. Eq 15 is restricted to dilute systems in which the interaggregate interactions can be ignored.

Since the density function (D_i) takes the maximum i value (i_{max}) at $\partial D_i/\partial i = 0$, i_{max} is expressed as:

$$i_{max} = (fe^{\alpha})^{1/2} = N_n \qquad (16)$$

i_{max} is equal to the number-average aggregation number (N_n). Thus, the monomer—monomer bond energy $\alpha\kappa T$ in the one-dimensional aggregation model can be calculated from

$$\alpha\kappa T = [\ln(N_n{}^2/f)]\kappa T \qquad (17)$$

This equation means that the energy of intermolecular hydrophobic bonding, contributing to formation of an aggregate, is determined by the N_n and f values at constant temperature.

For the hydrogen-bonded self-assembly systems of L-glutamic acid benzyl esters[39] in dioxane or benzene and L-leucyl glycine oligopeptides[40] in water, the plot of the $\alpha\kappa T$ value per peptide residue ($\alpha\kappa T/N_p$) against the residue number (N_p) for the two aggregate systems[39,40] was made using the SANS or NMR spin—lattice relaxation data of the concentrated sample solutions, furnishing an excellent linear relationship between $\alpha\kappa T/N_p$ and N_p.

The strength of most hydrogen bonds is in the energy range of 10—40 kJ mol^{-1}, which makes them stronger than a typical van der Waals force (~1 kJ mol^{-1}). All the $\alpha\kappa T$ values obtained were approximately in this range and are exactly equal to the hydrogen bond energies.

Thus, the results demonstrate that the one-dimensionally stacked rod-like aggregates become unstable with an increase in residue number (N_p), until an aggregate structure may finally be broken at N_p larger than the limiting value. That is, as a result of a decrease in the $\alpha\kappa T/N_p$ value, the contribution of intermolecular hydrogen bonding to the formation of the rod-like supra-molecular aggregates may become very low or zero. This restriction implies that the shape of an aggregate may be maintained until its size attains the limiting value and that variation of the shape may occur beyond that limit.

In order to apply the relation of eq 16 to the data shown in Figure 6, the origin was shifted to the inflection point I$_1$ (Figure 6A). Therefore, we may assume that a minimal TLM of HDeP grows along the linear-line from I$_1$ to I$_2$ (Region II) until the formation of RLAs starts to occur at an inflection point I$_2$. If the interaggregate interactions were neglected, the straight line from I$_1$ to I$_2$ follows eq 16. Similarly, when the inflection point I$_2$ is regarded as the origin, the growth of RLA progresses along the straight line from I$_2$ to I$_3$ (Region III), indicating that variation of n in this linear region holds for eq 16 (interaggregate interactions were also neglected).

Similar considerations were also made for the data shown in Figure 6B: the origins in region II′ and III′ were placed at the points I′$_1$ and I′$_2$, respectively. It was assumed that the n values of regions II′ and III′ increased approximately linearly with an increase in $(X - X_{cmc})^{1/2}$ and that the data in Figure 6B followed eq 16.

Based on considerations mentioned above, we concluded that eqs 16 and 17 were able to be applied to the aggregate systems of DAPs without interaggregate interactions.

A TLM structure may be regarded as a supra-molecular aggregate consisting of i unit-monomers (unit: one spheroidal micelle) stacked one-dimensionally with a hydrophobic bonding energy equal to $\alpha\kappa T$, assuming that the interaggregate interactions can be ignored.

For HDeP and HCeP, attempts to calculate $\alpha\kappa TN_A/n$ (E) were made by using SANS data (n: number-average aggregation number and N_A: Avogadro's number). We may regard this E value as the apparent energy, since the E value does not contain the contribution of interaggregate interactions. Thus, the apparent E value may be used as an indicator of variation of hydrophobic bonding energy in the process of the micelle growth.

The following assumptions were also made: (1) for HDeP, only TLMs contribute to their SANS spectral intensities in region II and only RLAs contribute to the intensities in region III; (2) for HCeP, only TLMs contribute to their SANS intensities in region II′. The contributions of spheroidal micelles, various vesicles, and others coexisting with the TLMs were neglected. The apparent E values, thus calculated for HDeP and HCeP, are listed in Table 2.

Table 2. Extracted E Values for HDeP (Regions II and III), HDoP (Region II),[24] and HCeP (Region II′)

sample	C/mol l^{-1}	n	E (kJ/mol)
	HDeP		
	3.10×10^{-2}	32	1.28
	3.30×10^{-2}	37	1.11
	4.60×10^{-2}	41	1.01
II	5.40×10^{-2}	45	0.90
	5.40×10^{-2}	45	0.90
	6.03×10^{-2}	53	0.78
	6.59×10^{-2}	60	0.69
III	7.40×10^{-2}	68	0.64
	HDoP*[a]		
	4.50×10^{-2}	109	0.38
	6.00×10^{-2}	177	0.24
II	7.40×10^{-2}	220	0.20
	HCeP		
	2.34×10^{-2}	207	0.22
	3.04×10^{-2}	306	0.15
	3.51×10^{-2}	354	0.13
II′	4.68×10^{-2}	370	0.13

[a]Asterisk for HDoP refers to ref 24.

For HDoP, similar attempts were also made using the SANS data reported in a previous paper,[24] based on the assumption that TLMs were elongated with an increase in concentration and became dominant above the second cmc (4.00×10^{-2} mol/l). The calculated E values are also listed in Table 2.

The E values obtained for HDeP, HCeP, and HDoP are in the energy range of a typical van der Waal's force, *ca* 1 kJ/mol. Thus, the E value may be regarded as an indicator of the energy valuation of interaggregate hydrophobic bonds required to form TLMs (or RLAs).

The plots of E against n in region II or II′ for HDeP, HDoP, and HCeP provided an excellent linear relationship (Figure 7). This linear relationship means that the apparent energy (E) of hydrophobic bonds per monomer, among the monomers in the
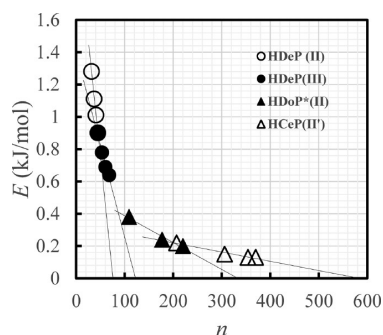
Figure 7. Plots of the E ($\alpha\kappa TN_A/n$) value against the number-average aggregation number (n) for HDeP (regions II (empty circles) and III (filled circles)), HDoP (region II (filled triangles)),[27] and HCeP (region II' (empty triangles)).

aggregate, decreases linearly with an increase in n. By inserting an extrapolated energy value of zero into this linear relationship, we can estimate the number-average aggregation number at $E = 0$. For HDeP, HDoP, and HCeP, E became zero at $n = 76$, 326, and 558, respectively, indicating that the contribution of interaggregate hydrophobic bonding to the formation of a TLM becomes zero at these aggregation numbers. We may conclude that a limiting size close to these aggregation numbers exists in the TLMs. However, since this result should also depend on assumptions as noted above, the actual size may be much greater, and there must be a distribution of sizes among TLMs.

The magnitude of the slope of a straight line in this plot may be also used as an indicator of variation in the energy of interaggregate hydrophobic bonding due to elongation of the TLM. An absolute value of the slope was found to increase in the order HDeP > HDoP > HCeP. This order implies that, for HDeP, reduction of the interaggregate hydrophobic bonding energy due to elongation of its TLM is greater than that for the TLM of HDoP or HCeP, due to a difference in the extent of hydration of the hydrocarbon chains between HDeP and HCeP (or HDoP),[24] as speculated from the SANS analyses (Table 1). Thus, an increase in the extent of hydration results in a reduction in the apparent E value.

It is likely that solvent molecules are embedded into "grooves" of the aggregate, weakening the formation of hydrophobic bonding between the monomers. This concept successfully explained the aggregation behavior of L-glutamic acid benzylester oligopeptides in dioxan.[39]

Existence of a limiting size in a TLM explains successfully the phenomenon of its breakage. When TLMs grow beyond a limiting size, shorter TLM-fragments with various sizes may be produced as a result of their breakage, together with many excess spheroids. TLMs having a distribution in size may retain their structures until their sizes attain the limiting values.

From the SANS results, in which the n values of TLMs in region II or II' tend to increase in the order HDeP < HDoP < HCeP, we may assume that a limiting size for each of the DAPs also increases in this order.

Eq 17 was also applied to the aggregate system in region III (RLA-growing region) for HDeP. The E against n in this region gave linear plots (Figure 7), implying that the interaggregate hydrophobic bonding energy for the formation of an RLA decreases linearly and rapidly with an increase in n. It was presumed that E became zero at an n value equal to 123, which corresponds to the estimated limiting size of a RLA, showing

that a RLA is broken at about that size. The actual sizes must be very much greater than this n value.

Thus, the interaggregate hydrophobic interaction energies forming an RLA or highly ordered RLAs may be very small, inducing a spontaneous RLA→Vesicle transition, mentioned above.

Models of a Lamellar Structure. In cryo-TEM images of aged DAP samples, it was confirmed that the transition of TLMs to RLAs occurred in higher concentrated samples in the isotropic phase (region I). Therefore, we may assume for HDeP that further growth of RLAs in region I led to the appearance of a lamellar microsolid, resulting in the phase-separation as a lamellar phase with an increase in concentration.

The X-ray diffraction patterns of the lyotropic liquid crystalline samples for HDeP (1.5, 1.8 and 2.4 mol/l) (Table 3) and HCeP (0.5 mol/l) were collected at 298 K, to evaluate

Table 3. Reciprocal of Volume Percentage[a] **(Φs(%)) and Spacing (d(Å)) of Small-Angle X-ray Diffraction Peaks for HDeP (Figure 8) in the Liquid Crystalline Region**

C (mol/l)	$1/\Phi s$	spacing[b] (d/Å)		
		1	2	3
1.5	2.22	38.2	19.1	9.1
1.8	1.85	32.5	16.1	10.7
2.4	1.56	28.4	14.3	9.1

[a]Volume percentage of surfactant: $\Phi_s(\%) = 100\,V_s/(V_w + V_s)$. V_s and V_w are volumes of surfactant and water, respectively. [b]These values are characteristics of a lamellar and were indexed to (001), (002), and (003), respectively.

the structures of various aggregates produced by asymmetric DAPs. The small-angle diffraction pattern of the HDeP sample (1.8 mol/L), as a representative example, is shown in Figure 8.
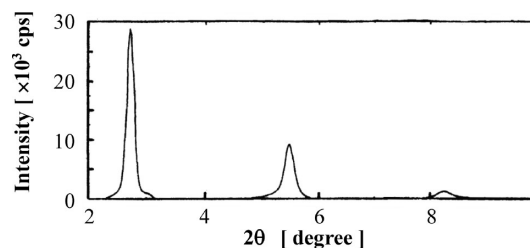

Figure 8. Observed X-ray diffraction pattern of the HDeP-H_2O (1.8 mol/l).

The diffraction patterns of the HDeP samples were characterized by a series in the order 1, 1/2, 1/3[41] and were assigned to a lamellar phase. The patterns in the concentration range 0.9−1.5 mol/L were not observed because of their very weak intensities. The spacing (d) indexed to (001) corresponds to the repeat distance involving a water layer in the lamellar structure. The value of spacing (d) tends to increase with decreasing concentration, indicating an increased thickness of the water layer. The d value is related to the surfactant concentration by Kotlarchyk−Huang−Kim−Chen's equation[42] $d = 2t/\varphi_s$ (t, the thickness of one hydrocarbon layer in a lamellar; φ_s, the volume fraction of the hydrocarbon part in a lamellar). The $d - 1/\varphi_s$ plots provided an excellent straight line ($d = 17.5\,(1/\varphi_s) + 0.05$), meaning a thickness $2t$ equal to 17.5 Å. The intercept 0.05 Å is consistent with the predicted intercept of zero expected for a lamellar phase.

Two models of type A (a closely packed model)[31,43] and type B (a loosely packed model)[31,43] were introduced to explain the thickness 17.5 Å. In type A, the two alkyl chains forming a bilayer are closely packed in a manner which alternatively combines short and long *n*-alkyl chains (Figure 9a). Conversely,
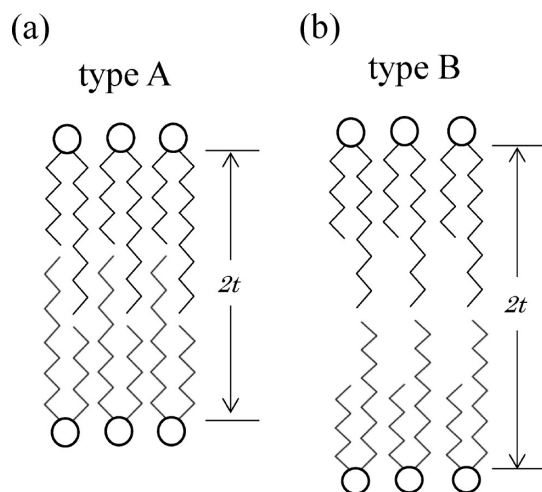

Figure 9. Schematic models of a lamellar ordering for HDeP or HCeP: type A (a), type B (b).

in type B, only the long *n*-alkyl (decyl) chains of the two surfactant molecules contribute to formation of a bilayer (Figure 9b). The thickness of a lamellar for HDeP was calculated: $2t = 20.2$ Å for type A and $2t = 25.8$ Å for type B. The lengths of *n*-decyl and *n*-hexyl chains were calculated using Tanford's equation ($L_{max} = 1.5 + 1.265n_c$; L_{max}, the maximum length of a hydrocarbon chain; n_c, the number of CH_2 group).[44] The *n*-hexyl and *n*-decyl chains were assumed to take up the all-*trans* conformations. This assumption is reasonable, since the probability of taking such extended hydrocarbon chains is high in shorter hydrocarbon chains. The thickness (17.5 Å) of a lamellar for HDeP is much smaller than that (25.8 Å) of type B, nor is it really close to that (20.2 Å) of type A. The application of a tilted lamellar concept[45] provided a satisfactory result. That is, in the HDeP lamellar membrane, the hydrocarbon parts ($2t$ = 17.5 Å) packed closely may be tilted with an angle $\theta = 58°$ normal to the W/O interface.

For the HCeP sample, the X-ray diffraction pattern (spacing $d/Å$: 37.4, 18.7, 12.4) characteristic of a lamellar and characterized by a series in the order 1: 1/2: 1/3,[41] was obtained and provided the thickness in a lamellar equal to 21.7 Å. Based on the assumption that the *n*-hexyl chain takes up the extended form while the *n*-cetyl chain prefers the gtg-kink form, the $2t$ values in the types A and B models were also calculated using Tanford's equation.[44] The calculated $2t$ values (28.3 Å for type A and 41.0 Å for type B) are much larger than that predicted by the X-ray diffraction method. To explain this disagreement, we also propose a tilted closely packed model with $2t = 21.7$ Å and the tilt angle $\theta = 50°$.

We may apply these tilted closely packed models to the structures of various lamellar membranes formed by HDeP and HCeP.

For asymmetric surfactants, in which one of the two hydrocarbon chains is shorter, interdigitation of the chains may contribute to such a smaller thickness in the lamellar. However, considering the fact that the all-*trans* chain effect of *n*-decyl chains upon aggregation is larger than that of *n*-cetyl

chains,[24,43] the interdigitation effect on the lamellar thickness of HCeP may be greater than that for HDeP.

A lamellar structure formed by a lipid or its analogous surfactants is generally accepted to exhibit a fully liquid-like behavior.[46] In the cryo-TEM images of HDeP (Figure 4A), the uni- and multilamellar vesicles seem to be flexible. The flexibility of a lamellar membrane may be associated with complicated correlation among layer elasticity, undulations,[47] and electrostatic interactions, making its origin very difficult to understand.

However, we point out the extreme asymmetry of a DAP molecule as one of the factors contributing to the flexibility. In a DAP lamellar, since we may assume the molecular motion (piston-like motion) lies along the direction of the main long hydrocarbon chain through a type with conformation intermediate between those of type A and type B, this motion may promote undulations contributing to the lamellar flexibility.

TLMs as Hydrated Polymers, TLM-Network and RLAs as Hydrated Associating Polymers, Their Orientated Structures and Phase-Transition. The complex, dynamic behavior of asymmetric DAP aggregates can be accounted for by the following concepts and models (Scheme II).

(1) Formation of TLMs and their growth beyond the limiting size occur even at low concentrations below the second cmc.

(2) A TLM does not break cooperatively. Its breakage occurs successively, as each one reaches the limiting size or grows beyond this size.
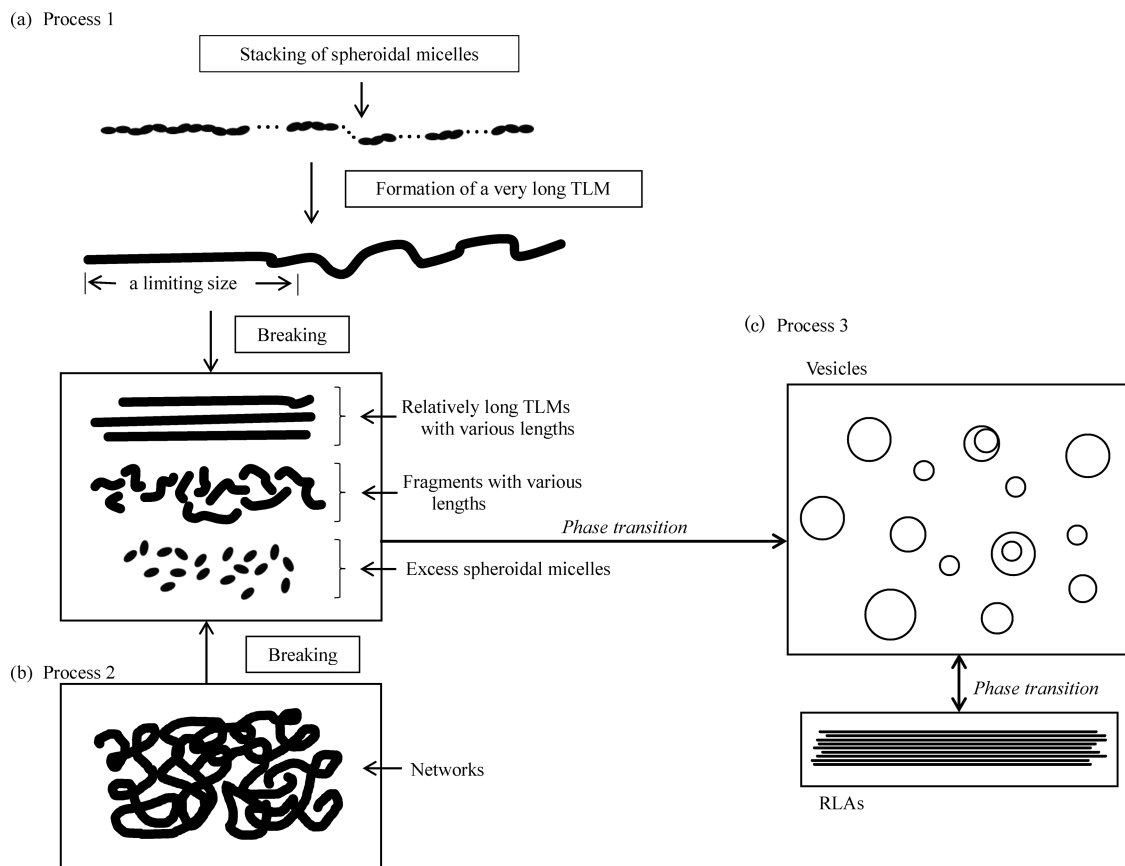
A TLM may be defined as a hydrated polymer stacked one-dimensionally by many spheroidal micelles fused together (one spheroid: an elemental unit) (Scheme IIa). Breakage of very long, flexible TLMs results in TLMs close to their limiting sizes, their fragments, and excess spheroidal micelles on the background of spheroidal micelles.

The network of TLMs existing as hydrated associating polymers may be regarded as a reflection of a gel-structure constituted of very long hydrated polymers interacting with each other through hydrogen bonding. Since hydrogen bonding between such hydrated polymers may be very weak,[39,40] the networks may be easily collapsed by thermal movement (Scheme IIb). The breakage of such a network also brings about the products similar to those mentioned above (gel→sol transition).

Consequently, breaking of very long, flexible TLMs or of networks changes the solute-concentration locally in the solution. The concentration gradient thus formed triggers the water-flow from the concentrated area to the dilute area (Marangoni convection).[48] Convective flowing may cause orderly alignment of thin, slender RLAs or that of extended TLMs toward different directions, and may also contribute to deformation of the vesicles due to acting of the dynamic pressure on their interfaces (Figure 4).

Of the products formed by the breakage of very long and flexible TLMs, many of extended TLMs may be transformed to RLA-structures driven by the orientation effect coming from the convective flowing (TLM→RLA transition).

The Marangoni convection analyses of a polymer-solution droplet have shown that a convective circulation flow, depending upon the concentration-ingredient, was predominant inside the droplet.[49] This result may be applicable to the present TLMs as hydrated polymers.

Scheme II. Models of Formation and Breaking of Hydrated DAP-Polymers[a]

[a](a) Process 1: As the concentration of a DAP surfactant increases above the first cmc, formation of spheroidal micelles occurs, together with their growth and stacking, and then molecular-diffusion among the stacked species leads to formation of TLMs with various lengths. However, the molecular size (length) of a TLM limits the size (number-average aggregation number n) of the aggregates, since the hydrophobic bonding energy between the monomer and the monomer in the aggregate decreases with an increase in n. Thus, a TLM beyond the limiting size may be broken, providing fragments of various sizes. (b) Process 2: The networks of TLMs (hydrated associated polymers) may be easily collapsed by thermal movement. The networks may be regarded as a gel of TLMs associated through hydration and their structure may be very weak so as to be easily broken by thermal movement or external forces (Ref 51). (c) Process 3: Fragments and excess spheroidal micelles formed by breaking of networks and very long TLMs may become seeds, leading to phase transitions for formation of vesicles and ribbons Since molecular aggregates of DAPs are not immobile but are virtually in a dynamic mobile state, degradation of the aggregate structures and re-construction or re-compilation from their fragments easily occurs, possibly inducing phase transition toward formation of various vesicles and ribbons (Ref 52).

The average constant spacing (11−13 nm) among thin, slender RLAs is in a range corresponding to smaller lamellar separations (2.5−22 nm), which probably originates from the summation of the hydration and van der Waal's contributions,[50] in addition to the electrostatic interactions among negatively charged DAP bilayers.

In a sol-phase produced immediately after the breakage of TLM or its network, shorter fragments with various sizes may play an important role as a nucleus and initiate the phase transition to uni- and multilamellar vesicles (Scheme IIc). A vesicle-phase thus appearing again is further transformed into the microsolid RLA lamellar phase. Furthermore, the RLA-phase causes again spontaneous, very slow transition to the vesicle phase. The hydration effect and TLM-fragments with spontaneous curvatures characteristic of the sizes may contribute to this series of transformation (Vesicle → RLA transitions).

In the cryo-TEM images of DAPs, after breaking of very long, flexible TLMs or its networks, multiphases, such as RLAs, unilamellar and multilamellar vesicles, disk-like flat lamellar, as well as TLMs and its fragments, seem to coexist under the background of spheroidal micelles. This behavior may be regarded as characteristic of hydrated asymmetric DAP-aggregate systems.

Further theoretical studies aimed at explaining the coexistence of multiphases[51,52] formed by asymmetric surfactants in aqueous solution are highly desirable.

■ CONCLUSIONS

The microstructures of extremely asymmetric DAPs in isotropic aqueous solutions were examined by cryo-TEM, SANS, and X-ray diffraction techniques. The concentration- and time-dependent cryo-TEM direct images provided evidence for the complex and dynamic changes of various aggregates, depending upon the length of the main long-hydrocarbon chain in a DAP. Using the average aggregation numbers of aggregates obtained from the SANS analyses, the energies of interaggregate hydrophobic bonding were calculated by application of the one-dimensional aggregate theory. Consequently, complex and dynamic changes of the DAP-aggregates were explained successfully by introduction of a model "the limiting size" in a TLM or a RLA. The existence of a limiting size causes

breaking of a TLM or an RLA and becomes a trigger of the phase transition to vesicles or disk-like structures. The lamellar models of various aggregates formed by asymmetric DAPs were estimated by the X-ray diffraction patterns of the lyotropic liquid crystalline samples.

Finally, models to explain the complex and dynamic changes of the aggregates were presented.

■ AUTHOR INFORMATION

Corresponding Authors
*ishi@tx.technion.ac.il
*h.okabayashi@nitech.jp

ORCID
Hiro-Fumi Okabayashi: 0000-0002-0132-6251

Notes
The authors declare no competing financial interest.

■ REFERENCES

(1) Luzzati, V. *X-ray Diffraction Studies of Lipid-Water System. Biological Membranes: Physical Fact and Function*; Chapman, D., Ed.; Academic Press: London, 1968; pp 71−123.

(2) Bendedouch, D; Chen, S. -H.; Koehler, W. C. Determination of Inter-particle Structure Factors in Ionic Micellar Solutions by Small Angle Neutron Scattering. *J. Phys. Chem.* **1983**, *87*, 2621−2628.

(3) Rand, R. P.; Fuller, N. L.; Gruner, S. M.; Parsegian, V. A. Membrane Curvature, Lipid Segregation, and Structural Transitions for Phospholipids under Dual-Solvent Stress. *Biochemistry* **1990**, *29*, 76−87.

(4) Jönson, B.; Lindman, B.; Holmberg, K.; Kronberg, B. *Surfactants and Polymers in Aqueous Solution*; John Wiley & Sons: New York, 1998, pp 1−380.

(5) de-Gennes, P. G. *Scaling Concepts in Polymer Physics*; Cornell University: Ithaca, 1979.

(6) Kawakatsu, K.; Kawasaki, K. Hybrid Models for the Dynamics of an Immiscible Binary Mixture with Surfactant Molecules. *Phys. A* **1990**, *167*, 690−735.

(7) van den Tempel, M.; Lucassen-Reynders, E. H. Relaxation Processes at Fluid Interfaces. *Adv. Colloid Interface Sci.* **1983**, *18*, 281−301.

(8) Germasheva, I. I.; Panaeva, S. A. Surface-Active Properties of Sulfosuccinate Solusions. *Kolloid. Zh.* **1982**, *44*, 592−596.

(9) Lucassen, J.; Drew, M. G. B. The Crystal Structure of Sodium Diheptylsulphosuccinate Dihydrate and Comparison with Phospholipids. *J. Chem. Soc., Faraday Trans. 1* **1987**, *83*, 3093−3106.

(10) Franses, E. I.; Puig, J. E.; Talmon, Y.; Miller, W. G.; Scriven, L. E.; Davis, H. T. Roles of Liquid Crystal and Micelles in Lowering Interfacial Tension. *J. Phys. Chem.* **1980**, *84*, 1547−1556.

(11) Nicolis, G.; Prigogine, I. *Self-Organization in Non-equilibrium Systems*; John Wiley & Sons: New York, 1977.

(12) Sumino, Y.; Kitahata, H.; Shinohara, Y.; Yamada, N.; Seto, H. Formation of a Multi-Scale Aggregate Structure through Spontaneous Blebbing of an Interface. *Langmuir* **2012**, *28*, 3378−3384.

(13) Kotlarchyk, M.; Chen, S. -H.; Huang, J. S.; Kim, M. W. Structure of Dense Sodium Di-2-Ethylhexylsulfosuccinate/D$_2$O/Decane Microemulsions. *Phys. Rev. Lett.* **1984**, *53*, 941−944.

(14) Sheu, E. Y.; Chen, S. -H.; Huang, J. S.; Sung, J. C. Non-Exponential Relaxations in Dense Micro-emulsion near the Glasslike Transition. *Phys. Rev. A: At., Mol., Opt. Phys.* **1989**, *39*, 5867−5876.

(15) Chen, S. -H.; Chang, S. -L.; Strey, R. Structural Evolution within the One-Phase Region of a Three-Component Microemulsion System: Water-*n*-Decane-Sodium Di-2-Ethylhexylsulfosuccinate (AOT). *J. Chem. Phys.* **1990**, *93*, 1907−1918.

(16) Eastoe, J.; Robinson, B. H.; Steytler, D. C. Influence of Pressure and Temperature on Microemulsion Stability. *J. Chem. Soc., Faraday Trans.* **1990**, *86*, 511−517.

(17) Seto, H.; Okuhara, D.; Kawabata, Y.; Takeda, T.; Nagao, M.; Suzuki, J.; Kamikubo, H.; Amemiya, Y. Pressure and Temperature Effects on the Phase Transition from a Dense Droplet to a Lamellar Structure in a Ternary Microemulsion. *J. Chem. Phys.* **2000**, *112*, 10608−10614.

(18) Ghosh, S. K.; Ichiyanagi, N.; Okabayashi, H. -F.; Yoshino, A.; Takeda, T.; O'Connor, C. J. Effect of Hydration on the Very Slow Droplet-Lamellar Transition in Di-Oleylsulfosuccinate/Decane/Water System: A Small Angle X-ray Scattering Study. *Bull. Chem. Soc. Jpn.* **2009**, *82*, 664−674.

(19) Yoshino, A.; Okabayashi, H. -F.; Yoshida, T.; Kushida, K. Dynamic Structure and Chirality Effects on ^{1}H and ^{13}C NMR Chemical Shifts for Aerosol OT in Reversed Micelles Assisted by NOESY, ROESY, and ^{13}CT$_1$ Studies. *J. Phys. Chem.* **1996**, *100*, 9592−9597.

(20) Mitchell, D. J.; Ninham, B. W. Micelles, Vesicles and Microemulsions. *J. Chem. Soc., Faraday Trans. 2* **1981**, *77*, 601−629.

(21) Hirata, H.; Katayama, S.; Okabayashi, H. -F.; Furusaka, M.; Kawakatsu, T. A Small-Angle Neutron Scattering Study of the Ethyl (*n*-Octyl) Phosphate Micelles in Water. *Colloid Polym. Sci.* **1996**, *274*, 245−252.

(22) Streefland, L.; Wagenaar, A.; Hoekstra, D.; Engberts, J. B. F. N. Effect of Alkyl Chain Aymmetry on the Fusion and Crystallization Behavior of Vesicles Formed from Di-n-Alkyl Phosphates. *Langmuir* **1993**, *9*, 219−222.

(23) Smits, E.; Blandamer, M. J.; Briggs, B.; Cullis, P. M.; Engberts, J. B. F. N. The Effect of Chain Flexibility on the Properties of Vesicles Formed from Di-n-Alkyl Phosphates. *Recl. Trav. Chim. Pays-Bas* **1996**, *115*, 37−43.

(24) Sasuga, S.; Weihs, D.; Talmon, Y.; Okabayashi, H. -F.; O'Connor, C. J. Aggregate Structures of Asymmetric Di-Alkyl Phosphate Anions and the Role of Conformations about the Polar Region: SANS, Cryo-TEM, Raman Scattering, ^{13}C NMR and Selective NOE Studies. *J. Phys. Chem. B* **2012**, *116*, 3538−3550.

(25) McCombie, H.; Saunders, B. C.; Stacey, G. J. Esters Containing Phosphorus. Part I. *J. Chem. Soc.* **1945**, *380−382*.

(26) Bellare, J. R.; Davis, H. T.; Scriven, L. E.; Talmon, Y. Controlled Environment Vitrification System: An Improved Sample Preparation Technique. *J. Electron Microsc. Tech.* **1988**, *10*, 87−111.

(27) Sears, V. F. Neutron Scattering Lengths and Cross Sections. *Methods of Experimental Physics*; Academic Press: London, 1986; Vol.23, Part A, pp 521−550.

(28) Bendedouch, D.; Chen, S. -H.; Koehler, W. C. Determination of Inter-particle Structure Factors in Ionic Micellar Solutions by Small Angle Neutron Scattering. *J. Phys. Chem.* **1983**, *87*, 2621−2628.

(29) Hayter, J. B.; Penfold, J. An Analytic Structure Factor for Macroion Solutions. *Mol. Phys.* **1981**, *42*, 109−118.

(30) Kotlarchyk, M.; Chen, S. -H. Analysis of Small Angle Neutron Scattering Spectra from Polydisperse Interacting Colloids. *J. Chem. Phys.* **1983**, *79*, 2461−2469.

(31) Sasuga-Araki, S.; Suzuki, K.; Okabayashi, H. -F.; O'Connor, C. J. Aggregate Structures of Asymmetric Di-Alkyl Phosphate Anions in Concentrated Aqueous Solutions and the Role of the Short Chain: X-ray Diffraction and Raman Scattering Studies. *Colloid Polym. Sci.* **2013**, *291*, 1927−1932.

(32) Winterhalter, M.; Lasic, D. D. Liposome Stability and Formation: Experimental Parameters and Theories on the Size Distribution. *Chem. Phys. Lipids* **1993**, *64*, 35−43.

(33) Laughlin, R. G.; Munyon, R. L.; Burns, J. L.; Coffindaffer, T. W.; Talmon, Y. Physical Science of the Di-octadecyldimethylammonium Chloride-Water System. 3. Colloidal Aspects. *J. Phys. Chem.* **1992**, *96*, 374−383.

(34) Lerebours, B.; Wehrli, E.; Hauser, H. Thermodynamic Stability and Osmotic Sensitivity of Small Unilamellar Phosphatidylcholine Vesicles. *Biochim. Biophys. Acta, Biomembr.* **1993**, *1152*, 49−60.

(35) Etori, H.; Hirata, H.; Yamada, Y.; Okabayashi, H. -F.; Furusaka, M. Micelle Formation of *N*-Decanoylglycine and *N*-Dodecanoyl−L-alanine Oligomer Potassium Salts and the Micellar Structure. *Colloid Polym. Sci.* **1997**, *275*, 263−273.

(36) Kline, S. R. Reduction and Analysis of SANS and USANS Data using IGOR Pro. *J. Appl. Crystallogr.* **2006**, *39*, 895−900.

(37) Missel, P. J.; Mazer, N. A.; Benedek, G. B.; Young, C. Y.; Carey, M. C. Thermodynamic Analysis of the Growth of Sodium Dodecylsulfate Micelles. *J. Phys. Chem.* **1980**, *84*, 1044−1057.

(38) Israelachvili, N. J. *Intermolecular and Surface Forces*, 2nd ed.; Academic Press: New York, 1991; p 341.

(39) Ishida, M.; Takai, M.; Okabayashi, H. -F.; Masuda, H.; Furusaka, M.; O'Connor, C. J. Supramolecular Aggregates Formed by L-Glutamic Acid Oligomers: SANS and SAXS Studies of the Hydrogen Bonded Self-Assembly. *Phys. Chem. Chem. Phys.* **2001**, *3*, 3140−3149.

(40) Yoshino, A.; Okabayashi, H. -F.; Kanbe, H.; Suzuki, K.; O'Connor, C. J. Folded Structures of L-Leucylglycine Oligopeptides and their Aggregational Behavior in Aqueous Solutions: Raman Scattering Spectra and Proton NMR Spin-Lattice Relaxation Studies. *J. Phys. Chem. B* **2008**, *112*, 5824−5833.

(41) Lipka, G.; Hauser, H. On the Phase Behavior of Lipid X, A Precursor of Bacterial Lipopolysaccharides. *Surfactants in Solutions*; Mittal, K. L., Shah, D. O., Eds.; Plenum Press: New York, 1991; Vol.*11*, pp 185−195.

(42) Kotlarchyk, M.; Huang, J. S.; Kim, M. W.; Chen, S.-H. Analysis of SANS Data from Dense Microemulsions. In *Surfactants in Solutions*; Mittal, K. L., Bothorel, P., Eds.; Plenum Press: New York, 1986; Vol. *6*, pp 1303−1314.

(43) Hirata, H.; Maegawa, K.; Kawamatsu, T.; Kaneko, S.; Okabayashi, H. -F. Phase Diagrams and Phase Structures of Identical and Mixed Chain Lithium Di-n-Alkyl Phosphate-Water Binary Systems: Asymmetric Molecular Shape Effect. *Colloid Polym. Sci.* **1996**, *274*, 654−661.

(44) Tanford, C. Micelle Shape and Size. *J. Phys. Chem.* **1972**, *76*, 3020−3024.

(45) Tsori, Y.; Andelman, D. Surface Induced Ordering in Thin Film Diblock Copolymers: Tilted Lamellar Phases. *J. Chem. Phys.* **2001**, *115*, 1970−1978.

(46) Sackman, E. Physical Basis of Self-Organization and Function of Membranes: Physics of Vesicles. In *Handbook of Biological Physics*; Lipowsky, R., Sackman, E., Eds.; Elsevier Science B. V., 1995; Vol. *1*, pp 213−303.

(47) Helfrich, W. Effect of Thermal Undulations on the Rigidity of Fluid Membranes and Interfaces. *J. Phys. (Paris)* **1985**, *46*, 1263−1268.

(48) Hu, H.; Larson, R. G. Evaporation of a Sessile Droplet on a Substrate. *J. Phys. Chem. B* **2002**, *106*, 1334−1344.

(49) Kaneda, M.; Hyakuta, K.; Takao, Y.; Ishizuka, H.; Fukai, J. Internal Flow in Polymer Solution Droplets Deposited on a Lyophobic Surface during a Receding Process. *Langmuir* **2008**, *24*, 9102−9109.

(50) Demé, B.; Dubois, M.; Zemb, T.; Cabane, B. Coexistence of Two Lyotropic Lamellar Phases Induced by a Polymer in a Phospholipid-Water System. *Colloids Surf., A* **1997**, *121*, 135−143.

(51) Matsuyama, A.; Tanaka, F. Theory of Solvation-Induced Reentrant Phase Separation in Polymer Solutions. *Phys. Rev. Lett.* **1990**, *65*, 341−344.

(52) Tanaka, F.; Koga, T. Molecular Aggregation of Polymers and Gelation (written in Japanese). *Research Institute for Mathematical Science* **1999**, *1081*, 58−65.